

# Unlocking the potential of atomic Ni reactive sites through interlayer confinement towards solar-to-hydrogen conversion from water

Yiming Zhang<sup>a,b</sup>, Xusheng Wang<sup>c,e,f,\*</sup>, Shibo Shao<sup>d</sup>, Xuefeng Lu<sup>a</sup>, Chenchen Feng<sup>a</sup>, Henan Jia<sup>a</sup>, Shunqin Luo<sup>b,\*\*</sup>, Jinhua Ye<sup>b,g,\*\*\*</sup>

<sup>a</sup> State Key Laboratory of Advanced Processing and Recycling of Non-ferrous Metal, School of Materials Science and Engineering, Lanzhou University of Technology, Lanzhou 730050, PR China

<sup>b</sup> International Center for Materials Nanoarchitectonics (WPI-MANA), National Institute for Materials Science (NIMS), 1-1 Namik, Tsukuba, Ibaraki 305-0044, Japan

<sup>c</sup> School of Materials Science and Engineering, Zhejiang Sci-Tech University, Hangzhou 310018, PR China

<sup>d</sup> Petrochemical Research Institute, PetroChina Company Limited, Beijing 102206, PR China

<sup>e</sup> Key Laboratory of Green Cleaning Technology & Detergent of Zhejiang Province, Lishui, Zhejiang 323000, PR China

<sup>f</sup> Guangdong Provincial Key Laboratory of Functional Supramolecular Coordination Materials and Applications, Jinan University, Guangzhou 510632, PR China

<sup>g</sup> TJU-NIMS International Collaboration Laboratory, School of Material Science and Engineering, Tianjin University, Tianjin 300072, PR China



## ARTICLE INFO

### Keywords:

Atomically isolated Ni  
Polydopamine interlayer  
Photocatalytic H<sub>2</sub> production  
Charge transfer

## ABSTRACT

The atomization of active sites on photocatalysts facilitates a pronounced interaction with reactants, yet achieving a precise manipulation of the coordination environment of reactive atomic center remains challenging. Herein, we innovatively adopted polydopamine framework as an interlayer to maximize the density of Ni atomic sites, forming a unique atomic arrangement of Ni–N<sub>4</sub> motif over CdS that delivers a remarkable photocatalytic H<sub>2</sub> evolution of 44.34 mmol/h/g. DFT calculations, corroborated by experimental analyses, suggest an electron-deficient nature of isolated Ni which can facilitate a facile adsorption and local polarization of H<sub>2</sub>O molecules. The distinctive polydopamine interlayer not only serves as a new charge transfer channel, but also optimize the interaction between Ni sites and critical intermediates, rendering a prompt recombinative desorption of \*H. This study offers unique perspectives on the collaborative interaction between the interlayer and the atomic active site, emphasizing their exceptional synergy for application in effective and sustainable catalytic conversions.

## 1. Introduction

Solar-light-driven water splitting using inorganic semiconductors for hydrogen (H<sub>2</sub>) generation provides a promising avenue toward solving the global energy crisis and combating environmental issues [1,2]. Nevertheless, the limited surface-active sites and inherently fast charge recombination in the most of inorganic photocatalysts kinetically result in suboptimal performance for solar-to-H<sub>2</sub> evolution [3–5]. Employing suitable cocatalysts can effectively accelerate the charge separation and migration, pumping photo-induced charge carriers from semiconductor to specific chemical bonds of adsorbates for facilitating surface reactant conversion [6–8]. For instance, our previous research exemplified the distinctive function of nickel oxide as active sites when combined with a

functional polymer layer, facilitating a favorable surface reaction [9]. In order to fully exploit the atomic utilization efficiency of cocatalysts, recent trend involves dispersing them at the atomic scale, thereby maximizing their activity by capitalizing on the abundance of active sites [10–13].

Atomically isolated non-precious nickel cocatalysts have demonstrated superior catalytic performance in promoting water splitting by not only increasing active sites but also providing sufficient light traps and accelerating charge transport efficiency [14–16]. However, considering the high surface energy and the lack of strong coordination environment, atomically isolated Ni is prone to growth and aggregation into clusters or even nanoparticles on the surface of an inorganic substrate compared to the organic counterpart [17–19]. Surface

\* Corresponding author at: School of Materials Science and Engineering, Zhejiang Sci-Tech University, Hangzhou 310018, PR China.

\*\* Corresponding author.

\*\*\* Corresponding author at: International Center for Materials Nanoarchitectonics (WPI-MANA), National Institute for Materials Science (NIMS), 1-1 Namik, Tsukuba, Ibaraki 305-0044, Japan.

E-mail addresses: [xswang@zstu.edu.cn](mailto:xswang@zstu.edu.cn) (X. Wang), [luoshunqin1116@163.com](mailto:luoshunqin1116@163.com) (S. Luo), [Jinhua.YE@nims.go.jp](mailto:Jinhua.YE@nims.go.jp) (J. Ye).

modification with functionalities for the inorganic semiconductor is generally needed to provide adequate sites for stabilizing single atoms, which requires multiple processes with harsh conditions [20–22].

Recent advances developed a facile coordination confinement strategy to embed the single metal atom into an organic/organic-inorganic hybrid framework [23,24], which enabled the construction of single-atom catalysts with precisely defined active site [25]. In order to tightly wrap the inorganic substrate with isolated metal sites, it is of paramount importance to rationally choose a suitable anchoring framework that can bind substrate with atomic sites through specific coordination. Polydopamine (PDA), with numerous catechol and amino functional groups, facilitated the anchoring of atomically dispersed metal sites through the generation of a strong coordination environment [26–28]. Numerous earth-abundant single-atom catalysts relying on PDA framework demonstrated impressive catalytic performance, yet most of these studies focused on the electrochemical or thermocatalytic application [29–32]. We reason that it would be highly desirable to utilize PDA as conductive interlayer, which could not only induce the high dispersion of Ni single atoms on inorganic semiconductor photocatalysts, but also facilitate the charge transport between support and active site, ultimately delivering a further catalytic activity enhancement toward light-driven H<sub>2</sub> production.

Taking the CdS as a model inorganic semiconductor substrate, in this work, the PDA framework enabled atomic dispersion of Ni active site is achieved for the first time. In-situ polymerization of dopamine ensures a coordinational confinement of single Ni reactive center through the formation of a distinct atomic arrangement of Ni–N<sub>4</sub> motif on the surface of CdS, which is further confirmed by advanced characterizations including X-ray absorption spectroscopy and aberration-corrected transmission electron microscopy. The optimized catalysts deliver a robust photocatalytic H<sub>2</sub> evolution of 44.34 mmol/h/g with the apparent quantum efficiency of 24% at 420 nm. Theoretical calculation, corroborated by experimental analyses, suggests that the PDA can not only coordinate single Ni site but also endow it electron-deficient state to readily activate H<sub>2</sub>O into \*H intermediates. Furthermore, unique atomic arrangement of Ni–N<sub>4</sub> motif in PDA induces the optimal interaction between \*H, rendering a prompt recombinative desorption. These findings emphasize the importance of interlayer construction between inorganic semiconductor and atomically reactive center, expanding the horizons of research focused on developing single atom catalysts with multi-functional interlayer towards efficient and sustainable catalytic conversions.

## 2. Experimental section

### 2.1. The fabrication of Ni/PDA/CdS catalysts

Initially, 1 g of commercial CdS was thoroughly dispersed into the solution consisting of 38 mL of deionized water and 15 mL of ethanol, and then sonicated for 10 min. Subsequently, 0.8 mL NH<sub>3</sub>·H<sub>2</sub>O (25%–28%), 200 mg dopamine hydrochloride and various amount of nickel acetate (the mole ratio of Ni/Cd is 0.1%, 0.3%, 0.6%, 1%, 1.5%, 2%, 3%, 5% and 8%, respectively) were successively added into above solution. The mixed solution was magnetically stirred for 5 h, and then centrifuged and washed with deionized water and ethanol. Resulting products were collected by vacuum drying for 5 h at a temperature of 60 °C. For comparison, different amount of dopamine hydrochloride (50 mg, 100 mg, 300 mg) with 0.6% Ni/Cd mole ratios were also fabricated under the same conditions. Obtained products were named as x-Ni/PDA/CdS-t (x refers to mole ration of Ni/Cd, t is the amount of dopamine hydrochloride).

### 2.2. The fabrication of reference samples

To demonstrate the advantages of single-atomic Ni site embedded in PDA for promoting H<sub>2</sub> evolution, reference samples were also fabricated.

The fabrication strategy and process used for the reference samples were similar to that used for the 0.6%-Ni/PDA/CdS-200 photocatalyst. The PDA/CdS-200 sample was prepared without the addition of nickel acetate, while the 0.6%-Ni/PDA sample was produced without the introduction of commercial CdS. Pure PDA was treated without addition of both nickel acetate and commercial CdS. 0.6%-Ni/CdS sample was fabricated using the photo-deposition strategy.

### 2.3. Photocatalytic performance evaluation

The photocatalytic H<sub>2</sub> evolution measurement was conducted using a closed glass reactor equipped with the gas circulation system. A visible light source, specifically 300 W Xenon lamp with an L42 cutoff filter, was used to excite the photocatalytic H<sub>2</sub> evolution. In this experiment, 5 mg sample was evenly dispersed into 20 mL solution of Na<sub>2</sub>S (0.25 M) and Na<sub>2</sub>SO<sub>3</sub> (0.35 M). Before the photocatalytic reaction, the reaction cell was evacuated for 20 min to remove air completely. The generated H<sub>2</sub> was automatically quantified by an on-line gas chromatography equipped with thermal conductivity detector (GC-TCD, GC-8A, Japan) using Ar as carrier gas. Each measurement was conducted continuously for 3 h, and photocatalytic stability was evaluated using the same procedure. In addition, the apparent quantum efficiency (AQE) was measured under the irradiation of monochromatic light in different wavelengths (420 nm, 440 nm, 460 nm, 480 nm, 500 nm, 520 nm, 540 nm, 560 nm, and 600 nm, respectively) using corresponding optical filters. AQE was calculated according to the following equation:

$$\text{AQE of H}_2\text{ production} = \frac{\text{number of evolved H}_2\text{ molecules} \times 2}{\text{number of incident photons}} \times 100\%$$

## 3. Results and discussion

### 3.1. Synthesis and structural characterizations

A facile strategy was adopted to embed single Ni atoms within a polydopamine (PDA) interlayer that wraps around the CdS semiconductor. The dopamine is selected as key monomer to coordinate Ni ions and then in-situ polymerized over CdS to form single-atomic Ni site under alkaline conditions. An amorphous nature of pure PDA and 0.6%-PDA, as revealed by X-ray diffraction (XRD) patterns, results in similar characteristic diffraction peaks with hexagonal CdS (JCPDS No. 06-0314) for CdS, PDA/CdS-200 and 0.6%-Ni/PDA/CdS-200 (Figure S1). The appearance of absorption peak at 1638 cm<sup>-1</sup> (C=C stretching vibrations of the benzene ring) and 1106 cm<sup>-1</sup> (characteristic peak for CdS) in PDA/CdS-200 and 0.6%-Ni/PDA/CdS-200 samples suggest that the dopamine was successfully polymerized to form PDA on the CdS semiconductor (Figure S2) [33]. The SEM images of the pure PDA and Ni dispersed PDA present the nanosphere appearance (Figure S3a and b); when atomically isolated Ni dispersed PDA wraps around the CdS, a roughened surface of 0.6%-Ni/PDA/CdS-200 can be observed (Figure S3c–e).

Transmission electron microscopy (TEM) images of 0.6%-Ni/PDA/CdS-200 clearly demonstrate the single-atomic Ni arranged PDA that tightly wraps around the CdS, forming an ultrathin and amorphous layer with a thickness of approximately 17 nm (Fig. 1a and S4b). The high-angle annular dark-field scanning transmission electron microscopy (HAADF-STEM) images of 0.6%-Ni/PDA/CdS-200 sample (Fig. 1b and c) confirm the dispersion of single-atomic Ni (bright dots circled by red due to their higher atomic number compared to PDA substrate), and these single atoms are evenly distributed throughout the entire PDA framework. No Ni nanoparticles were observed within the PDA layers in different area, suggesting that atomic Ni sites may be uniformly embedded within the PDA layers (Figure S4c–e). Additionally, energy dispersive X-ray spectroscopy (EDX) elemental mapping of the 0.6%-Ni/PDA/CdS-200 sample elucidates that atomically dispersed Ni sites are

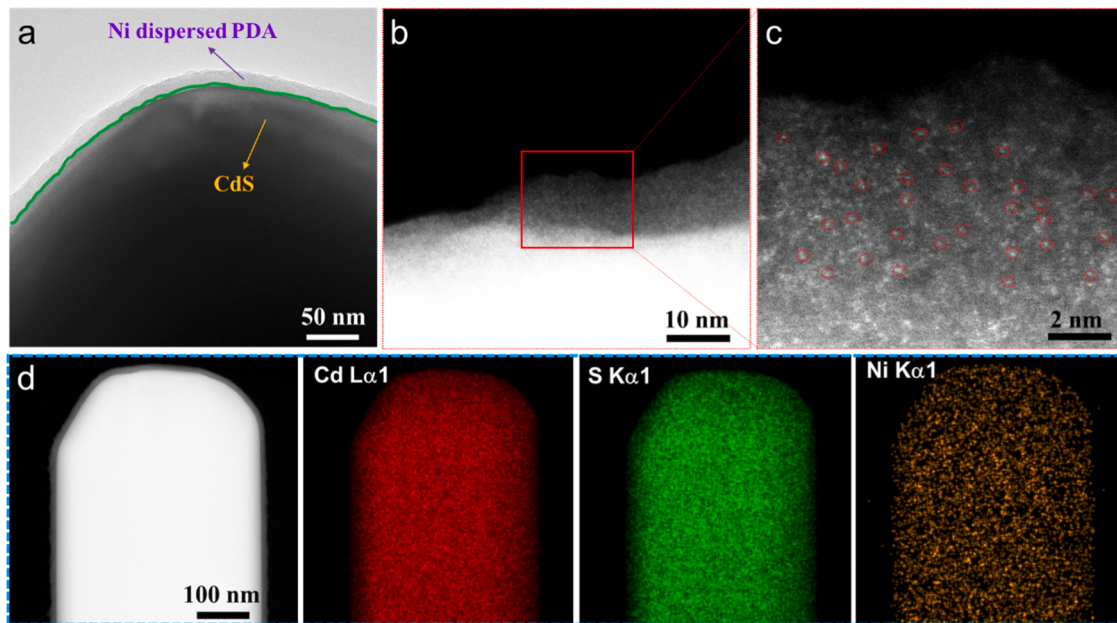


**Fig. 1.** (a) HRTEM images of 0.6%-Ni/PDA/CdS-200. (b) HAADF-STEM, and (c) Corresponding high-resolution HAADF-STEM image of 0.6%-Ni/PDA/CdS-200, Ni atoms are highlighted by red circles. (d) STEM-EDS mapping of 0.6%-Ni/PDA/CdS-200.

uniformly distributed across the entire CdS (Fig. 1d) without noticeable aggregation. These results concordantly indicate that single-atomic Ni sites have been successfully embedded into PDA, which may serve as a highly active cocatalyst.

In order to provide a comprehensive insight into the coordinational characteristics and local geometric structure of isolated Ni sites in PDA, X-ray absorption spectroscopy measurements were conducted. Ni X-ray absorption near edge structure (XANES) spectrum of 0.6%-Ni/PDA/CdS-200 shows the absorption edge approaching to that of NiO, suggesting that the Ni species mainly exist the valence state of Ni<sup>2+</sup> (Fig. 2a) [34].

In addition, the extended X-ray absorption fine structure (EXAFS) oscillation in the *R* space of 0.6%-Ni/PDA/CdS-200 exhibits main characteristic features for the Ni–N(O) coordination without obvious Ni–Ni bond, indicating the atomically isolated Ni site that may coordinate with N or O atoms of PDA (Fig. 2b). Wavelet transform (WT) contour plots further verify this assumption, as displayed in Fig. 2c, the maximum intensity appears at approximately 4.8 Å<sup>-1</sup> for the planar Ni–N(O) coordination in single-atomic Ni arranged PDA, which is different from Ni–Ni bond (6–8 Å<sup>-1</sup> in Ni foil) and Ni–O bond (3–4 Å<sup>-1</sup> in NiO), implying that Ni atoms may mostly coordinate with

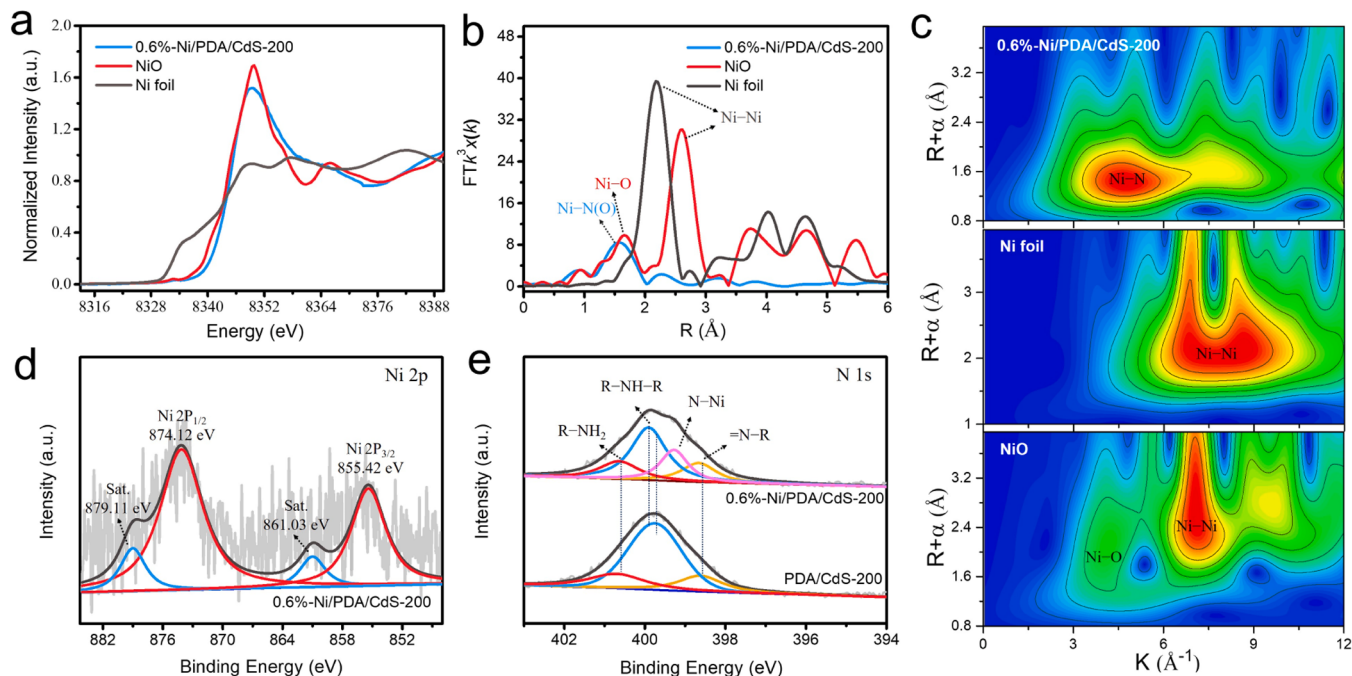


**Fig. 2.** (a) Normalized Ni K-edge XANES spectra and (b)  $k^3$ -weighted Fourier transformed spectra from Ni K-edge EXAFS of 0.6%-Ni/PDA/CdS-200, Ni foil, and NiO standard sample. (c) The wavelet analysis of Fourier-transform EXAFS of 0.6%-Ni/PDA/CdS-200, Ni foil and NiO. High-resolution XPS spectra of (d) Ni 2p and (e) N 1s.

N. Specific characteristics for the local coordination of central Ni atom can be obtained by fitting the EXAFS. As shown in Figure S5 and Table S1, the average coordination number (CN) of Ni is approximately 4, corresponding to the Ni–N<sub>4</sub> units with the average bond length of 2.05 Å.

Additionally, X-ray photoelectron spectroscopy (XPS) is used to characterize the chemical states of Ni, N, C and O elements. The Ni 2p core-level peaks at 874.12 and 855.42 eV in the 0.6%-Ni/PDA/CdS-200 could assign to the positive valence state of Ni<sup>2+</sup> (Fig. 2d) [35], which agree well with XANES results. The N 1 s spectrum of 0.6%-Ni/PDA/CdS-200 can be evolved into peaks corresponding to R–NH<sub>2</sub> (400.68 eV), R–NH–R (399.93 eV), Ni–N (399.22 eV) and =N–R (398.64 eV) (Fig. 2e) [36–38]. It is evident that the R–NH–R peak of the 0.6%-Ni/PDA/CdS-200 sample shifts towards a higher binding energy and its signal fraction greatly decreases compared to PDA/CdS-200. This result further indicates that the nitrogen atom at R–NH–R could bond with Ni<sup>2+</sup> to generate Ni–N coordination in single-atomic Ni arranged PDA. Meanwhile, the C 1 s (Figure S6) and O 1 s (Figure S7) spectrum of PDA/CdS-200 and 0.6%-Ni/PDA/CdS-200 sample show no significant difference. The O 1 s spectrum displays two peaks at 531.35 and 532.94 eV, which were assigned to C=O (partial oxidization of hydroxyl into quinone) and C–O species [39]. The absence of a Ni–O signal further implies that the Ni<sup>2+</sup> typically coordinate with the N atoms. Based on the above structural and chemical analysis, the most stable coordination structure is proposed (Figure S8), which contains Ni–N<sub>4</sub> coordination that stabilized by PDA interlayer.

### 3.2. Photocatalytic performance for H<sub>2</sub> evolution

Photocatalytic behavior for H<sub>2</sub> evolution was evaluated using Na<sub>2</sub>SO<sub>3</sub>/Na<sub>2</sub>S as the sacrificial reagent. As shown in Fig. 3a, the H<sub>2</sub> evolution rates over x-Ni/PDA/CdS-200 with different Ni contents are investigated. Interestingly, the H<sub>2</sub> evolution rate rapidly increase with small Ni contents ranging from 0.1% to 0.6%, and then slowly reaches a plateau as the Ni content rises from 0.6% to 8%. The nickel-normalized activities stemming from average turnover frequencies (ATOF) are also calculated (Fig. 3b). It is revealed that the ATOF firstly keep constant

with increasing Ni content from 0.1% to 0.6%, and then drops sharply as the Ni content rises from 0.6% to 8%. Consequently, atomically dispersed Ni may display a constant atom utilization efficiency and rapidly increase H<sub>2</sub> evolution rate with the increasing Ni contents from 0.1% to 0.6%. Declined ATOF with the high Ni loading amount (> 0.6%) implies the decreased atom utilization efficiency, which could be attributed to the agglomeration of Ni. As a result, 0.6%-Ni/PDA/CdS-200 displays the maximum Ni atom utilization efficiency with attractive ATOF value of 977.5 h<sup>-1</sup>, delivering an outstanding H<sub>2</sub> production rate of 44.34 mmol/h/g which outperforms the most of CdS-based photocatalysts reported in recent years (Table S2).

The H<sub>2</sub> generation activity over 0.6%-Ni/PDA/CdS-x was measured to investigate the effect of dopamine amount on dispersing single Ni atom across CdS (Fig. 3c). The H<sub>2</sub> generation rate rises from 33.74 mmol/h/g to 44.34 mmol/h/g with increasing the dopamine amount from 50 mg to 200 mg, and then drops to 36.9 mmol/h/g with the maximum amount of 300 mg. Further structural characterizations illustrate that the excessive amount of PDA did not result in a distinctive dispersion of Ni active sites compared to the optimized case (Figure S9 to S12), albeit with its potential capacity to enhance light absorption and spatial separation of photo-induced charge carriers (Figure S13 and 14). However, excessive dosage of PDA may lead to a strong coverage over CdS, and consequently reduces H<sub>2</sub> evolution due to the shielding effect [40] (Supplementary Note 1).

To further prove the superiority of atomic arrangement of 0.6%-Ni/PDA/CdS-200 on boosting performance, controlled experiments were conducted using pure CdS, 0.6%-Ni/CdS, PDA/CdS-200, 0.6%-Ni/PDA and PDA. As presented in Fig. 3d, the H<sub>2</sub> evolution rate of 0.6%-Ni/PDA/CdS-200 is 4.2 times as high as that of pure CdS, and is 170 and 341 times of 0.6%-Ni/PDA and PDA, respectively. Meanwhile, photocatalytic H<sub>2</sub> evolution rate of 0.6%-Ni/PDA/CdS-200 is higher than that of PDA/CdS-200. In addition, compared to 0.6%-Ni/PDA/CdS-200, the 0.6%-Ni/CdS sample fabricated using the photo-deposition strategy exhibits a relatively lower photocatalytic H<sub>2</sub> evolution rate due to the aggregation of Ni (Figure S15), suggesting the single-atomic Ni plays the crucial role as the active sites on H<sub>2</sub> evolution. Apparent quantum efficiencies (AQE) under the irradiation of monochromatic light in different

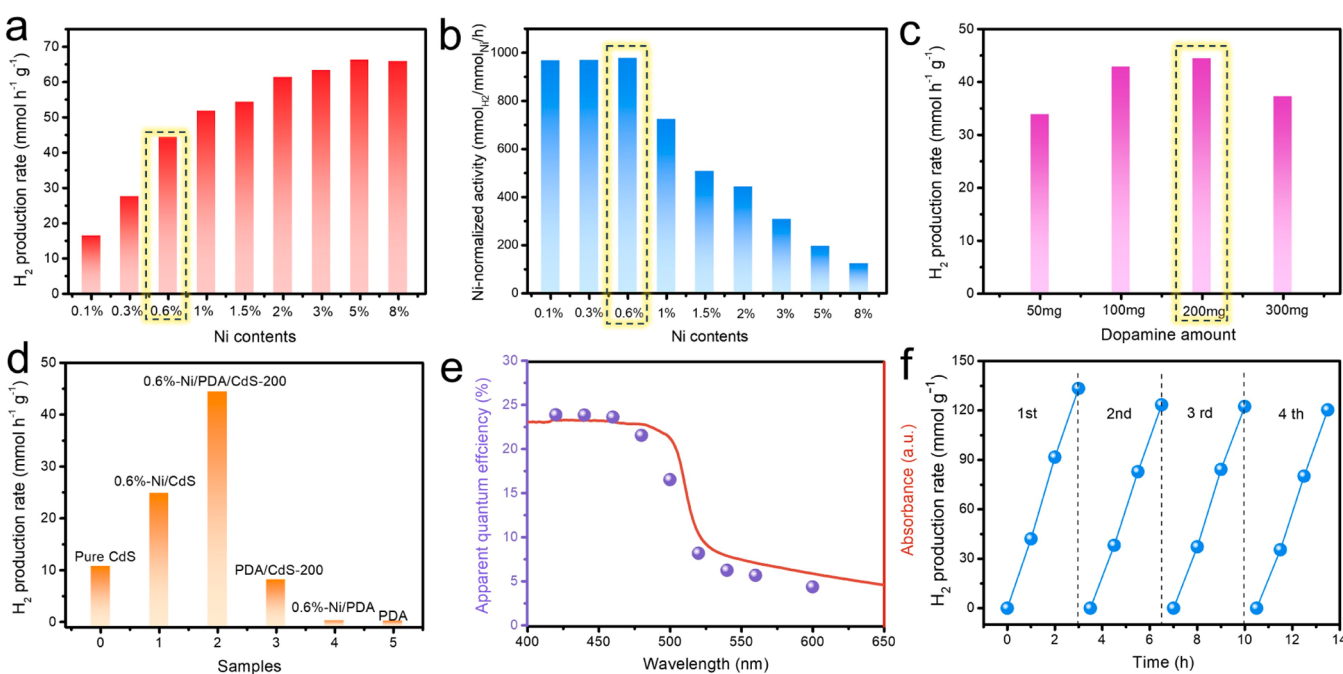


**Fig. 3.** (a) H<sub>2</sub> evolution rate over x-Ni/PDA/CdS-200 with different Ni contents. (b) Ni-normalized H<sub>2</sub> evolution rate in x-Ni/PDA/CdS-200 sample. (c) The effect of dopamine additive amount on H<sub>2</sub> evolution rate in 0.6%-Ni/PDA/CdS-x. (d) H<sub>2</sub> evolution rate compared with reference sample. (e) Wavelength-dependent AQE of photocatalytic H<sub>2</sub> evolution over 0.6%-Ni/PDA/CdS-200. (f) Stability of 0.6%-Ni/PDA/CdS-200 for H<sub>2</sub> evolution.

wavelengths show similar trend with light absorption spectra of 0.6%-Ni/PDA/CdS-200 (Fig. 3e), reaching a notable value of 24% under 420 nm monochromatic light irradiation. The light intensity and the corresponding H<sub>2</sub> production rate at different band-pass filters were presented in Table S3. Furthermore, 0.6%-Ni/PDA/CdS-200 exhibits a long-term stability in recycling tests with 5 mg (Fig. 3f) and 100 mg sample (Figure S16) and produces an almost stable catalytic performance in four cycles.

### 3.3. Charge-carrier dynamics

Optical and electrochemical properties was investigated to discover origin on boosting H<sub>2</sub> evolution for single-atomic Ni arranged PDA cocatalyst. The UV-vis absorption spectra (Fig. 4a) shows that the CdS encapsulated with PDA remarkably strengthen absorption across the whole visible light range compared to pure CdS. When the atomically dispersed Ni is embedded into PDA, light-harvesting is further tamped due to efficient modulation of PDA electronic structure [41]. The corresponding bandgaps of CdS, PDA/CdS-200 and 0.6%-Ni/PDA/CdS-200 were calculated to be 2.40, 2.38 and 2.37 eV, respectively, using Kubelka-Munk function[42] (Fig. 4b). The photoluminescence (PL) emission spectra (Fig. 4c) reveal that 0.6%-Ni/PDA/CdS-200 with the weakest PL emission intensity could greatly restrain the charge recombination. It is also worth noting that the PL emission peak of PDA/CdS-200 and 0.6%-Ni/PDA/CdS-200 is located at 535 nm, whereas the peak of pure CdS is presented at 547 nm. The blue shift implies that the surface charger recombination in CdS is effectively suppressed, which might be because that a new charge transfer channel is generated through wrapping PDA or single-atomic Ni arranged PDA on CdS [43].

Meanwhile, the time-resolved photoluminescence (TRPL) is also adopted to elucidate the charge lifetimes and migration dynamics (Fig. 4d). The biexponential fitting of TRPL spectra of pure CdS, PDA/CdS-200 and 0.6%-Ni/PDA/CdS-200 are summarized in Table S4 [44]. The short lifetime ( $\tau_1$ ) can be ascribed to the radiative pathways, and 0.6%-Ni/PDA/CdS-200 display a relatively small  $\tau_1$  of 0.027 ns. This indicates that the single-atomic Ni arranged PDA cocatalyst could efficiently transfer photoexcited charge of CdS, thus reducing participation

in radiative recombination. The long lifetime ( $\tau_2$ ) (nonradiative energy decay processes) of 0.6%-Ni/PDA/CdS-200 is lower than that of PDA/CdS-200 and pure CdS. This suggests that PDA provides new charge transfer channel as the effective nonradiative decay pathway, and endows the single-atomic Ni with the highest attenuated transition rate. Moreover, the shortened average fluorescence lifetime ( $\tau_a$ ) in 0.6%-Ni/PDA/CdS-200 further implies that the PDA framework could rapidly move the carrier over CdS to the isolated Ni atom. The rate constant of electron transfer ( $k_{ET}$ ) (determined by  $k_{ET} = 1/\tau_{(composite)} - 1/\tau_{(CdS)}$ , where  $\tau$  is the average fluorescence lifetime [45]) in the 0.6%-Ni/PDA/CdS-200 are calculated to be 6.67 ns<sup>-1</sup>, which is 3.5 times as high as the PDA/CdS-200 (1.89 ns<sup>-1</sup>). This result suggests that the isolated Ni atom can serve as the mediator to greatly accelerate transfer of photogenerated carriers from CdS via the PDA framework.

In addition, Fig. 4e depicts the photocurrent responses of pure CdS, PDA/CdS-200 and 0.6%-Ni/PDA/CdS-200. Pure CdS exhibits the lower photocurrent intensity. After wrapping with PDA layers, the photocurrent intensity climbs apparently. The current intensity of 0.6%-Ni/PDA/CdS-200 is further increased compared to PDA/CdS-200. This indicates that PDA framework has a strong ability to accelerate charge transfer, and incorporating isolated Ni atom site can further promote charge separation. Moreover, electrochemical impedance spectroscopy (EIS) of 0.6%-Ni/PDA/CdS-200 illustrates a smaller the semicircle in Nyquist plots, which indicates a faster the electron transfer in the photocatalyst (Fig. 4f). The unique coordination structure of Ni sites produces a powerful driving force to lead the charger transfer from CdS to atomic centers, thus achieving ultrafast electron hopping. Based on above results, it is concluded that the superior photocatalytic H<sub>2</sub> evolution performance of 0.6%-Ni/PDA/CdS-200 is highly consistent with its outstanding photoelectric properties.

### 3.4. DFT calculation and mechanistic analysis

To understand how Ni single atom facilitates adsorption and activation of H<sub>2</sub>O molecules, the charge density differences (CDD) of Ni/PDA/CdS upon adsorbing H<sub>2</sub>O were simulated using density functional theory-based (DFT) calculation. Fig. 5a, b highlights the charge transfer (electron accumulation and depletion) and structure configuration

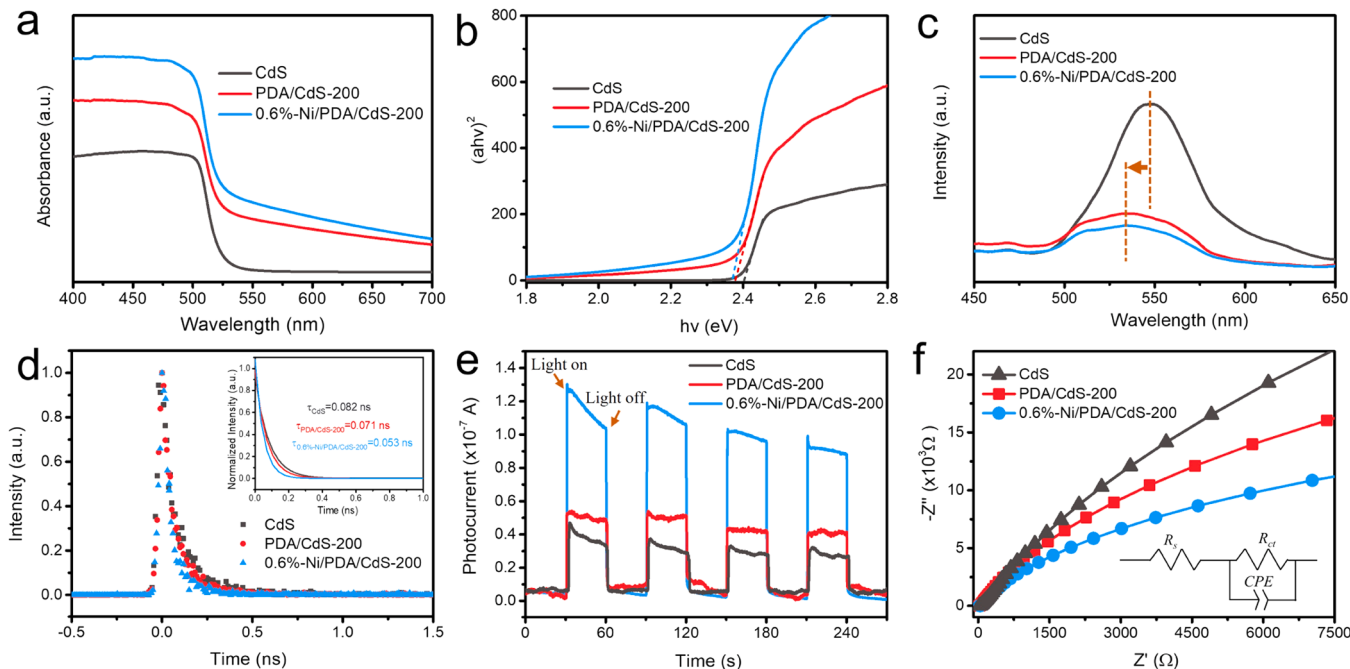


**Fig. 4.** (a) UV-vis. absorption spectra, (b) Calculated bandgap structures, (c) PL spectra, (d) Time-resolved transient PL decay spectra, (e) Transient photocurrent responses and (f) EIS spectra of CdS, PDA/CdS-200 and 0.6%-Ni/PDA/CdS-200 photocatalyst.

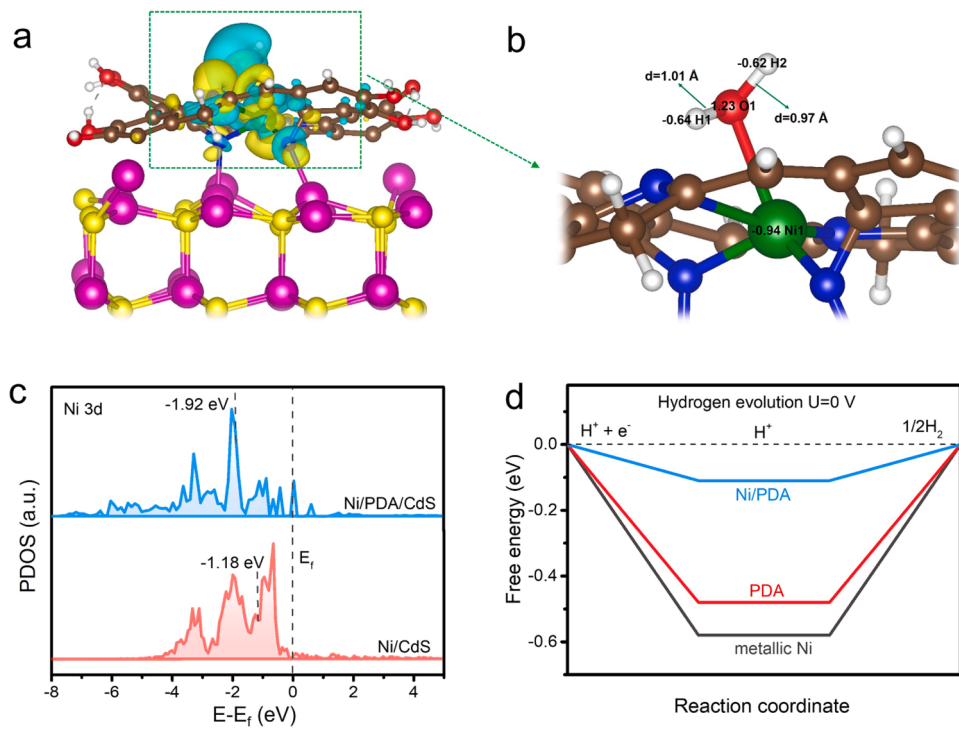


**Fig. 5.** (a) The charge density difference between the adsorbed H<sub>2</sub>O and Ni/PDA/CdS, yellow: charge accumulation, cyan: charge depletion, the value of isosurface is 0.0007 au. (b) Difference of charge density and bond length of H<sub>2</sub>O molecular over atomically isolated Ni active sites, (c) PDOS plots of Ni/CdS and Ni/PDA/CdS, (d) Calculated free energy profile for hydrogen evolution.

appears upon adsorption of H<sub>2</sub>O on the catalyst surface. A pronounced redistribution of charge densities between different components in H<sub>2</sub>O-Ni/PDA/CdS system can be observed (Fig. 5a, Figure S17, and Table S5). The Ni appears to be electron depleted, which may accelerate the spatial separation of photo-induced charge carriers. Moreover, the electron-deficient nature of Ni could trigger a facile adsorption of H<sub>2</sub>O[46] by endowing a robust electron exchange with the water molecule, thereby facilitating a rapid consecutive reaction step (H<sub>2</sub>O activation). Bader charge analysis of the optimized structure after H<sub>2</sub>O adsorption simulates the charge density difference as well as bond length of O-H in H<sub>2</sub>O\* on Ni active sites (Fig. 5b). Upon the adsorption, a significant charge redistribution can be observed within the H<sub>2</sub>O molecule, which might bring a local polarization for the H<sub>2</sub>O activation. Meanwhile, the bond length of O1-H1 (1.01 Å) is greatly elongated compared to that of O1-H2 (0.97 Å) upon the interaction with Ni active site, suggesting the activation of O-H bond for water dissociation through the interaction and charge donation from Ni active sites.

Above theoretical results suggest that the interactions between \*H<sub>2</sub>O and isolated Ni active sites could effectively adsorb and activate H<sub>2</sub>O molecules, producing \*H as the intermediate. The recombinative desorption of \*H produces H<sub>2</sub> as final product, therefore, adsorption/desorption of \*H also play a critical role in determining the overall catalytic performance. To gain a deeper understanding, the electronic structures of the atomically isolated Ni embedded in PDA and metallic Ni nanoparticle on CdS were studied using partial density of states (PDOS) calculation (Fig. 5c). Indeed, a downward shift of the d-band center of atomic Ni (-1.92 eV) produces a weaker interaction between \*H compared to the metallic Ni counterpart (-1.18 eV), suggesting that the desorption of \*H might be facilitated on single Ni active site.

DFT calculation is further adopted to investigate the hydrogen adsorption Gibbs free energy ( $\Delta G_H$ ). The calculation models of three kinds of cocatalysts including metallic Ni, pure PDA and atomically dispersed Ni coordinated PDA are shown in Figure S18. The H<sub>2</sub> evolution performance could be closely related with the Gibbs free energy of the adsorbed \*H ( $|\Delta G_{*H}|$ )[47], and  $|\Delta G_{*H}|$  value closing to 0 means the

optimal bond energy to hydrogen, indicating the cocatalyst favors to the hydrogen adsorption and consequent desorption in reactions[48]. As displayed in Fig. 5d, the single Ni atom embedded in PDA framework displays a much lower  $|\Delta G_{*H}|$  compared to metallic Ni and pure PDA. This result elucidates that the unique coordination environment of single-atomic Ni-N<sub>4</sub> active sites embedded in PDA framework could efficiently optimize adsorption-desorption energy of hydrogen on isolated Ni atom, which offer the highly favorable sites of H<sub>2</sub> generation for 0.6%-Ni/PDA/CdS-200.

A refined mechanism scheme is established to explain the optimal H<sub>2</sub> evolution process over CdS encapsulated with the single-atomic Ni arranged PDA. Under irradiation of visible light, CdS semiconductor would be firstly excited to generate photoelectrons and consequent transport to single-atomic Ni-N<sub>4</sub> sites via PDA framework, and also the superfluous electrons are stored by filling the outermost d orbital of Ni atom. Meanwhile, the H<sub>2</sub>O molecule adsorbed on isolated Ni active sites could be effectively dissociate into \*H. Ultimately, the enriched electrons on Ni active sites can quickly reduce the adsorbed hydrogen into H<sub>2</sub> and then release it. As a result, the redistributed the charge densities, the suitable d-band center value and the optimal hydrogen adsorption-desorption capacity of single-atomic Ni active site, collectively endow the 0.6%-Ni/PDA/CdS-200 the excellent photocatalytic H<sub>2</sub> evolution performance.

#### 4. Conclusion

In summary, PDA framework was adopted as an interlayer to enable atomic arrangement of Ni active site on the surface of CdS photocatalyst. We demonstrated that atomically dispersed Ni can bond with nitrogen of PDA, forming a Ni-N<sub>4</sub> motif in the PDA framework. Such an atomic architecture delivered a photocatalytic H<sub>2</sub> evolution rate of 44.34 mmol/h/g with an apparent quantum efficiency of 24% at 420 nm. The distinctive PDA interlayer can not only maximize Ni active site density but also provide a new charge transfer channel to facilitate the charge transport between support and atomically isolated Ni active

site. Moreover, the electron-deficient state of atomized Ni configurations facilitates a rapid consecutive activation of  $\text{H}_2\text{O}$  into  $^*\text{H}$  intermediates, and subsequently, the desorption of  $^*\text{H}$  can be optimized by PDA framework. The remarkable catalytic performance was attributed to the cooperative interaction between the PDA interlayer and the atomic Ni site, highlighting their excellent synergy as the key factor.

### CRediT authorship contribution statement

**Xuefeng Lu:** Investigation, Formal analysis. **Shibo Shao:** Investigation, Formal analysis. **Xusheng Wang:** Project administration, Funding acquisition, Formal analysis. **yiming zhang:** Writing – review & editing, Writing – original draft, Validation, Methodology, Investigation, Formal analysis, Conceptualization. **Jinhua Ye:** Writing – review & editing, Supervision, Project administration. **Shunqin Luo:** Supervision, Project administration, Data curation, Conceptualization. **Henan Jia:** Investigation, Formal analysis. **Chenchen Feng:** Investigation, Formal analysis.

### Declaration of Competing Interest

The authors declare that they have no known competing financial interests or personal relationships that could have appeared to influence the work reported in this paper.

### Data Availability

Data will be made available on request.

### Acknowledgement

This work was financially supported by the World Premier International Research Center Initiative (WPI Initiative) on Materials Nano-architectonics (MANA), MEXT (Japan), National Natural Science Foundation of China (Grant No. 22102066, 22362020, 52102102), the Natural Science Foundation of Gansu Province (No. 22JR5RA309), the Tamarisk Outstanding Young Talents Program of Lanzhou University of Technology in 2023 (No. 062308) and 2022 (No. 062211), the Open Fund of Guangdong Provincial Key Laboratory of Functional Supramolecular Coordination Materials and Applications (No. 2022A06).

### Appendix A. Supporting information

Supplementary data associated with this article can be found in the online version at [doi:10.1016/j.apcatb.2024.123893](https://doi.org/10.1016/j.apcatb.2024.123893).

### References

- [1] H. Nishiyama, T. Yamada, M. Nakabayashi, Y. Maehara, M. Yamaguchi, Y. Kuromiya, Y. Nagatsuma, H. Tokudome, S. Akiyama, T. Watanabe, Photocatalytic solar hydrogen production from water on a 100-m<sup>2</sup> scale, *Nature* 598 (2021) 304–307, <https://doi.org/10.1038/s41586-021-03907-3>.
- [2] P. Zhou, I.A. Navid, Y. Ma, Y. Xiao, P. Wang, Z. Ye, B. Zhou, K. Sun, Z. Mi, Solar-to-hydrogen efficiency of more than 9% in photocatalytic water splitting, *Nature* 613 (2023) 66–70, <https://doi.org/10.1038/s41586-022-05399-1>.
- [3] X. Shi, C. Dai, X. Wang, J. Hu, J. Zhang, L. Zheng, L. Mao, H. Zheng, M. Zhu, Protruding Pt single-sites on hexagonal  $\text{ZnIn}_2\text{S}_4$  to accelerate photocatalytic hydrogen evolution, *Nat. Commun.* 13 (2022) 1287, <https://doi.org/10.1038/s41467-022-28995-1>.
- [4] J. Ran, H. Zhang, S. Fu, M. Jaroniec, J. Shan, B. Xia, Y. Qu, J. Qu, S. Chen, L. Song, J.M. Cairney, L. Jing, S.Z. Qiao,  $\text{NiPS}_3$  ultrathin nanosheets as versatile platform advancing highly active photocatalytic  $\text{H}_2$  production, *Nat. Commun.* 13 (2022) 4600, <https://doi.org/10.1038/s41467-022-32256-6>.
- [5] M. Xiao, L. Zhang, B. Luo, M. Lyu, Z. Wang, H. Huang, S. Wang, A. Du, L. Wang, Molten-salt-mediated synthesis of an atomic nickel Co-catalyst on  $\text{TiO}_2$  for improved photocatalytic  $\text{H}_2$  evolution, *Angew. Chem. Int. Ed.* 59 (2020) 7230–7234, <https://doi.org/10.1002/anie.202001148>.
- [6] G.Z.S. Ling, S.F. Ng, W.J. Ong, Tailor-engineered 2D cocatalysts: harnessing electron-hole redox center of 2D g-C<sub>3</sub>N<sub>4</sub> photocatalysts toward solar-to-chemical conversion and environmental purification, *Adv. Funct. Mater.* 32 (2022) 2111875, <https://doi.org/10.1002/adfm.202111875>.
- [7] A.K. Singh, C. Das, A. Indra, Scope and prospect of transition metal-based cocatalysts for visible-light-driven photocatalytic hydrogen evolution with graphitic carbon nitride, *Coord. Chem. Rev.* 465 (2022) 214516, <https://doi.org/10.1016/j.ccr.2022.214516>.
- [8] J. Xiao, T. Hisatomi, K. Domen, Narrow-band-gap particulate photocatalysts for one-step-excitation overall water splitting, *Acc. Chem. Res.* 56 (2023) 878–888, <https://doi.org/10.1021/acs.accounts.3c00011>.
- [9] Y. Zhang, X. Wang, X. Ren, S. Luo, H. Huang, R. chen, S. Shao, D. Liu, J. Gao, J. Gui, J. Ye, Building rapid charge transfer channel via engineering Ni coordinated flexible polymer for efficient solar hydrogen evolution, *Chem. Eng. J.* 456 (2023) 141032, <https://doi.org/10.1016/j.cej.2022.141032>.
- [10] N. Denisov, S. Qin, J. Will, B.N. Vasiljevic, N.V. Skorodumova, I.A. Pasti, B. Sarma, B. Osuagwu, T. Yokosawa, J. Voss, J. Wirth, E. Speecker, P. Schmuki, Light-induced agglomeration of single-atom platinum in photocatalysis, *Adv. Mater.* 35 (2023) e2206569, <https://doi.org/10.1002/adma.202206569>.
- [11] H. Peng, T. Yang, H. Lin, Y. Xu, Z. Wang, Q. Zhang, S. Liu, H. Geng, L. Gu, C. Wang, X. Fan, W. Chen, X. Huang, Ru/In dual-single atoms modulated charge separation for significantly accelerated photocatalytic  $\text{H}_2$  evolution in pure water, *Adv. Energy Mater.* 12 (2022) 2201688, <https://doi.org/10.1002/aenm.202201688>.
- [12] Y. Huang, D. Li, S. Feng, Y. Jia, S. Guo, X. Wu, M. Chen, W. Shi, Pt Atoms/Clusters on Ni-phosphate-sensitized carbon nitride for enhanced NIR-light-driven overall water splitting beyond 800 nm, *Angew. Chem. Int. Ed.* 61 (2022) e202212234, <https://doi.org/10.1002/anie.202212234>.
- [13] Z.H. Xue, D. Luan, H. Zhang, X.W. Lou, Single-atom catalysts for photocatalytic energy conversion, *Joule* 6 (2022) 92–133, <https://doi.org/10.1016/j.joule.2021.12.011>.
- [14] L. Lin, Q. Yu, M. Peng, A. Li, S. Yao, S. Tian, X. Liu, A. Li, Z. Jiang, R. Gao, X. Han, Y.W. Li, X.D. Wen, W. Zhou, D. Ma, Atomically Dispersed Ni/alpha-MoC Catalyst for Hydrogen Production from Methanol/Water, *J. Am. Chem. Soc.* 143 (2021) 309–317, <https://doi.org/10.1021/jacs.0c10776>.
- [15] C. Zhang, H. Wang, H. Yu, K. Yi, W. Zhang, X. Yuan, J. Huang, Y. Deng, G. Zeng, Single-Atom Catalysts for Hydrogen Generation: Rational Design, Recent Advances, and Perspectives, *Adv. Energy Mater.* 12 (2022) 2200875, <https://doi.org/10.1002/aenm.202200875>.
- [16] L. Jiao, H.L. Jiang, Metal-organic-framework-based single-atom catalysts for energy applications, *Chem* 5 (2019) 786–804, <https://doi.org/10.1016/j.chempr.2018.12.011>.
- [17] M. Wang, S. Xu, Z. Zhou, C.L. Dong, X. Guo, J.L. Chen, Y.C. Huang, S. Shen, Y. Chen, L. Guo, Atomically dispersed janus nickel sites on red phosphorus for photocatalytic overall water splitting, *Angew. Chem. Int. Ed.* 61 (2022) e202204711, <https://doi.org/10.1002/anie.202204711>.
- [18] H. Choi, S. Oh, S.B.T. Tran, J.Y. Park, Size-controlled model Ni catalysts on Ga<sub>2</sub>O<sub>3</sub> for CO<sub>2</sub> hydrogenation to methanol, *J. Catal.* 376 (2019) 68–76, <https://doi.org/10.1016/J.JCAT.2019.06.051>.
- [19] Y. Wang, Y. Qu, B. Qu, L. Bai, Y. Liu, Z.D. Yang, W. Zhang, L. Jing, H. Fu, Construction of six-oxygen-coordinated single Ni sites on g-C<sub>3</sub>N<sub>4</sub> with Boron-Oxo species for photocatalytic water-activation-induced CO<sub>2</sub> reduction, *Adv. Mater.* 33 (2021) 2105482, <https://doi.org/10.1002/adma.202105482>.
- [20] S. Lv, M. Pei, Y. Liu, Z. Si, X. Wu, R. Ran, D. Weng, F. Kang, An isolation strategy to anchor atomic Ni or Co cocatalysts on TiO<sub>2</sub> (A) for photocatalytic hydrogen production, *Nano Res.* 15 (2022) 5848–5856, <https://doi.org/10.1007/s12274-022-4217-6>.
- [21] P. Liu, Z. Huang, S. Yang, J. Du, Y. Zhang, R. Cao, C. Chen, L. Li, T. Chen, G. Wang, Support amorphization engineering regulates single-atom Ru as an electron pump for nitrogen photofixation, *ACS Catal.* 12 (2022) 8139–8146, <https://doi.org/10.1021/acscatal.2c01704>.
- [22] P. Zhou, Q. Zhang, Z. Xu, Q. Shang, L. Wang, Y. Chao, Y. Li, H. Chen, F. Lv, Q. Zhang, L. Gu, S. Guo, Atomically dispersed Co-P<sub>3</sub> on CdS nanorods with electron-rich feature boosts photocatalysis, *Adv. Mater.* 32 (2020) e1904249, <https://doi.org/10.1002/adma.201904249>.
- [23] J.W.H. Zhang, J. Dong, G. Liu, L. Shi, P. An, G. Zhao, J. Kong, X. Wang, X. Meng, J. Zhang, J. Ye, Efficient visible-light-driven carbon dioxide reduction by a single-atom implanted metal-organic framework, *Angew. Chem. Int. Ed.* 55 (2016) 14310–14314, <https://doi.org/10.1002/anie.201608597>.
- [24] Q. Zuo, T. Liu, C. Chen, Y. Ji, X. Gong, Y. Mai, Y. Zhou, Ultrathin metal-organic framework nanosheets with ultrahigh loading of single Pt atoms for efficient visible-light-driven photocatalytic H<sub>2</sub> evolution, *Angew. Chem. Int. Ed.* 58 (2019) 10198–10203, <https://doi.org/10.1002/anie.201904058>.
- [25] T. He, S. Chen, B. Ni, Y. Gong, Z. Wu, L. Song, L. Gu, W. Hu, X. Wang, Zirconium-porphyrin-based metal-organic framework hollow nanotubes for immobilization of noble-metal single atoms, *Angew. Chem. Int. Ed.* 57 (2018) 3493–3498, <https://doi.org/10.1002/anie.201800817>.
- [26] W. Qu, S. Niu, D. Sun, H. Gao, Y. Wu, Z. Yuan, X. Chen, Y. Wang, T. An, G. Wang, Pb single atoms enable unprecedented catalytic behavior for the combustion of energetic materials, *Adv. Sci.* 8 (2021) 2002889, <https://doi.org/10.1002/advs.202002889>.
- [27] Y. Lu, H. Wang, P. Yu, Y. Yuan, R. Shahbazian-Yassar, Y. Sheng, S. Wu, W. Tu, G. Liu, M. Kraft, Isolated Ni single atoms in nitrogen doped ultrathin porous carbon templated from porous g-C<sub>3</sub>N<sub>4</sub> for high-performance CO<sub>2</sub> reduction, *Nano Energy* 77 (2020) 105158, <https://doi.org/10.1016/j.nanoen.2020.105158>.
- [28] K. Wang, Z. Lu, J. Lei, Z. Liu, Y. Li, Y. Cao, Modulation of ligand fields in a single-atom site by the molten salt strategy for enhanced oxygen bifunctional activity for zinc-air batteries, *ACS nano* 16 (2022) 11944–11956, <https://doi.org/10.1021/acsnano.2c01748>.

[29] H. Zhang, W. Zhou, X.F. Lu, T. Chen, X.W. Lou, Implanting isolated Ru atoms into edge-rich carbon matrix for efficient electrocatalytic hydrogen evolution, *Adv. Energy Mater.* 10 (2020) 2000882, <https://doi.org/10.1002/aenm.202000882>.

[30] C. Dong, C. Zhou, M. Wu, Y. Yu, K. Yu, K. Yan, C. Shen, J. Gu, M. Yan, C. Sun, Boosting Bi-directional redox of sulfur with dual metal single atom pairs in carbon spheres toward high-rate and long-cycling lithium-sulfur battery, *Adv. Energy Mater.* 13 (2023) 2301505, <https://doi.org/10.1002/aenm.202301505>.

[31] W. Xiong, H. Li, H. Wang, J. Yi, H. You, S. Zhang, Y. Hou, M. Cao, T. Zhang, R. Cao, Hollow mesoporous carbon sphere loaded Ni-N4 single-atom: support structure study for CO<sub>2</sub> electrocatalytic reduction catalyst, *Small* 16 (2020) 2003943, <https://doi.org/10.1002/smll.202003943>.

[32] L.N. Song, W. Zhang, Y. Wang, X. Ge, L.C. Zou, H.F. Wang, X.X. Wang, Q.C. Liu, F. Li, J.J. Xu, Tuning lithium-peroxide formation and decomposition routes with single-atom catalysts for lithium-oxygen batteries, *Nat. Commun.* 11 (2020) 2191, <https://doi.org/10.1038/s41467-020-15712-z>.

[33] W. Wang, M. Li, X. Huang, J. Fang, F. Peng, H. Huang, Structural evolution mechanisms of Polydopamine/CdS and photothermal effect boosted photocatalytic H<sub>2</sub> production activity, *Appl. Surf. Sci.* 601 (2022) 154114, <https://doi.org/10.1016/j.apsusc.2022.154114>.

[34] Y. Xiong, W. Sun, P. Xin, W. Chen, X. Zheng, W. Yan, L. Zheng, J. Dong, J. Zhang, D. Wang, Y. Li, Gram-scale synthesis of high-loading single-atomic-site Fe catalysts for effective epoxidation of styrene, *Adv. Mater.* 32 (2020) e2000896, <https://doi.org/10.1002/adma.202000896>.

[35] M. Kwak, J. Bok, B.H. Lee, J. Kim, Y. Seo, S. Kim, H. Choi, W. Ko, W.H. Antink, C. W. Lee, Ni single atoms on carbon nitride for visible-light-promoted full heterogeneous dual catalysis, *Chem. Sci.* 13 (2022) 8536–8542, <https://doi.org/10.1039/D2SC02174A>.

[36] P. Lu, Y. Yang, J. Yao, M. Wang, S. Dipazir, M. Yuan, J. Zhang, X. Wang, Z. Xie, G. Zhang, Facile synthesis of single-nickel-atomic dispersed N-doped carbon framework for efficient electrochemical CO<sub>2</sub> reduction, *Appl. Catal. B: Environ.* 241 (2019) 113–119, <https://doi.org/10.1016/j.apcatb.2018.09.025>.

[37] C. Cheng, S. Zong, J. Shi, F. Xue, Y. Zhang, X. Guan, B. Zheng, J. Deng, L. Guo, Facile preparation of nanosized MoP as cocatalyst coupled with g-C<sub>3</sub>N<sub>4</sub> by surface bonding state for enhanced photocatalytic hydrogen production, *Appl. Catal. B: Environ.* 265 (2020) 118620, <https://doi.org/10.1016/j.apcatb.2020.118620>.

[38] R. Shen, K. He, A. Zhang, N. Li, Y. Ng, P. Zhang, J. Hu, X. Li, In-situ construction of metallic Ni<sub>3</sub>C@Ni core-shell cocatalysts over g-C<sub>3</sub>N<sub>4</sub> nanosheets for shell-thickness-dependent photocatalytic H<sub>2</sub> production, *Appl. Catal. B: Environ.* 291 (2021) 120104, <https://doi.org/10.1016/j.apcatb.2021.120104>.

[39] Y. Kim, E. Coy, H. Kim, R. Mrówczyński, P. Torruella, D.W. Jeong, K.S. Choi, J. H. Jang, M.Y. Song, D.J. Jang, F. Peiro, S. Jurga, H.J. Kim, Efficient photocatalytic production of hydrogen by exploiting the polydopamine-semiconductor interface, *Appl. Catal. B: Environ.* 280 (2021) 119423, <https://doi.org/10.1016/j.apcatb.2020.119423>.

[40] C. Bie, B. Zhu, F. Xu, L. Zhang, J. Yu, In situ grown monolayer N-doped graphene on CdS hollow spheres with seamless contact for photocatalytic CO<sub>2</sub> reduction, *Adv. Mater.* 31 (2019) 1902868, <https://doi.org/10.1002/adma.201902868>.

[41] G. Wang, T. Zhang, W. Yu, Z. Sun, X. Nie, R. Si, Y. Liu, Z. Zhao, Efficient Electronic Modulation of g-C<sub>3</sub>N<sub>4</sub> Photocatalyst by Implanting Atomically Dispersed Ag1-N3 for Extremely High Hydrogen Evolution Rates, *CCS Chem.* 4 (2022) 2793–2805, <https://doi.org/10.31635/ccschem.021.202101191>.

[42] Y. Liu, Y. Sun, E. Zhao, W. Yang, J. Lin, Q. Zhong, H. Qi, A. Deng, S. Yang, H. Zhang, H. He, S. Liu, Z. Chen, S. Wang, Atomically dispersed silver-cobalt dual-metal sites synergistically promoting photocatalytic hydrogen evolution, *Adv. Funct. Mater.* 33 (2023) 2301840, <https://doi.org/10.1002/adfm.202301840>.

[43] T. Ye, P. Cheng, H. Zeng, D. Yao, X. Pan, H. Jiang, J. Ding, Pressure-induced bifurcation in the photoluminescence of red carbon quantum dots: coexistence of emissions from surface groups and nitrogen-doped cores, *J. Phys. Chem. Lett.* 13 (2022) 4768–4777, <https://doi.org/10.1021/acs.jpclett.2c01161>.

[44] C. Cheng, B. He, J. Fan, B. Cheng, S. Cao, J. Yu, An Inorganic/Organic S-Scheme Heterojunction H<sub>2</sub>-Production Photocatalyst and its Charge Transfer Mechanism, *Adv. Mater.* 33 (2021) e2100317, <https://doi.org/10.1002/adma.202100317>.

[45] B. He, C. Bie, X. Fei, B. Cheng, J. Yu, W. Ho, A.A. Al-Ghamdi, S. Wageh, Enhancement in the photocatalytic H<sub>2</sub> production activity of CdS NRs by Ag<sub>2</sub>S and NiS dual cocatalysts, *Appl. Catal. B: Environ.* 288 (2021) 119994, <https://doi.org/10.1016/j.apcatb.2021.119994>.

[46] M. Wu, R. Zhang, C. Li, X. Sun, G. Chen, L. Guo, K. Zheng, X. Sun, Optimizing strong metal-support interaction on cobalt phosphide-supported Ru single atom catalyst for highly-efficient hydrogen evolution reaction, *Mater. Chem. Front.* 7 (2023) 4918–4927, <https://doi.org/10.1039/d3qm00561e>.

[47] Q. Jin, N. Liu, C. Dai, R. Xu, Y. Du, H<sub>2</sub>-Directing Strategy on In Situ Synthesis of Co-MoS<sub>2</sub> with Highly Expanded Interlayer for Elegant HER Activity and its Mechanism, *Adv. Energy Mater.* 10 (2020) 2000291, <https://doi.org/10.1002/aenm.202000291>.

[48] Z. Li, J.Y. Fu, Y. Feng, C.K. Dong, H. Liu, X.W. Du, A silver catalyst activated by stacking faults for the hydrogen evolution reaction, *Nat. Catal.* 27 (2019) 1107–1114, <https://doi.org/10.1038/s41929-019-0365-9>.